Spatial characteristics and kinematics of floodplain aggradation cycles in the lower Eocene Bighorn Basin, Wyoming, USA

Youwei Wang[1,2], Timothy F. Baars[1], Joep E.A. Storms[1], Allard W. Martinius[1,3], Philip D. Gingerich[4], Magda Chmielewska[5], Simon J. Buckley[6], and Hemmo A. Abels[1]*

[1] Department of Geosciences and Engineering, Delft University of Technology, Stevinweg 1, 2628 CN Delft, the Netherlands

[2] Department of Environmental Sciences, University of Virginia, Charlottesville, VA 22903, USA

[3] Equinor ASA, Arkitekt Ebbellsvei 10, N–7053 Trondheim, Norway

[4] Museum of Paleontology, University of Michigan, Ann Arbor, MI 48109-1079, USA

[5] Department of Geology and Petroleum Geology, University of Aberdeen, Aberdeen AB24 3UE, UK

[6] NORCE Norwegian Research Centre AS, P.O. Box 22, N-5838 Bergen, Norway

**Correspondence email: youweiwang2021@outlook.com*

Abstract:

Interaction of allogenic and autogenic forcing in building alluvial stratigraphy remains a complex subject that is critical for paleoenvironmental and paleoclimate reconstruction and subsurface rock property prediction. Autogenic processes may act at similar vertical and lateral scales at which astronomical climate forcing drives alluvial stratigraphic deposition, making it difficult to disentangle these drivers in the rock record. In the lower Eocene Willwood Formation, Bighorn Basin, Wyoming, USA, a lot of evidence has been gathered to relate dominant floodplain aggradation cycles to precession-scale climate change. Previous studies have analyzed these cycles to be consistently developed in multiple areas of the basin of different ages and, in one study, in two parallel one-dimensional (1-D)

stratigraphic sections spaced several kilometers apart. However, the 3-D geometry of these floodplain aggradation cycles remains largely unknown. Building upon previous studies, these cycles are viewed to be driven by allogenic forcing in concert with autogenic factors in this research. Our goal is to reveal to what extent allogenic climate forcing produces regionally consistent sedimentary patterns and autogenic processes produce lateral variability. Here, 44 floodplain aggradation cycles were mapped and measured in 3-D space using an unmanned aerial vehicle (UAV) to develop a photogrammetric model covering a geographic area of *ca*10 km^2 and spanning a stratigraphic succession of *ca* 300 m. The 44 cycles have an average thickness of 6.8 m with a standard deviation of 2.0 m and a coefficient of variation of 29% in line with previous studies. Most cycles are consistently traceable over the entire model, indicating spatial consistency in line with previous studies exemplifying allogenic climate forcing by the climatic precession cycle. Individual floodplain aggradation cycles may change in thickness rapidly laterally, with rates up to 1 m over a lateral distance of 100 m and a maximum of 4 m. Detailed mapping of seven successive cycles that are extensively present in the outcrops reveals differences in their regionally-averaged thicknesses of 3.7 m to 9.7 m, with their coefficients of variation ranging between 17% and 28%. Variogram analysis demonstrates that the thickness of a cycle at one locality is significantly related to that at another locality within an average distance of 1.3 km in the paleoflow direction and 0.6 km perpendicular to the paleoflow direction. This is interpreted as a result of morphological elements oriented in paleoflow directions in the ancient fluvial landscapes shaping more consistency of the sedimentary elements in paleoflow directions. Strong thickness compensation of floodplain aggradation cycles is observed at 20-40 kyr time scales and full compensation occurs between 120 and 240 kyr. In compacted floodplain stratigraphy, the measured vertical scale of autogenic processes impacting stratigraphy is 4.0 to 5.2 m at 95% significance. This is below the scale of precession-climate drivers occurring at around 7.0 m thickness, which is probably why autogenic and allogenic drivers can be disentangled in this series.

Keywords: precession; floodplain aggradation cycle; compensational stacking; alluvial stratigraphy; Eocene; Bighorn Basin

1. INTRODUCTION

Alluvial stratigraphy is fundamentally controlled by channel avulsion frequency and long-term sediment accumulation rates (Allen, 1978) that are recorded by the distribution and configuration of channel sandstone bodies and coeval fine-grained sediment (Allen, 1978; Bridge & Leeder, 1979). Channels aggrade or prograde faster than surrounding non-channelized regions (Hajek & Wolinsky, 2012), causing avulsion to occur when a topographic threshold is exceeded (Karssenberg & Bridge, 2008; Mohrig *et al.*, 2000). Rates of aggradation or degradation are determined by accommodation and sediment supply. Superelevation may be reached with all settings stable due to continuous higher aggradation rates in the channel belts than in the floodplains. Regional river avulsions in these cases are fully autogenically controlled. Climate, tectonics, and base level may also impact these factors and speed up or slow down the rates at which superelevation is reached (Slingerland & Smith, 2004) or may trigger regional river avulsion at the time superelevation is (nearly) reached (Abels *et al.*, 2013).

Fluvial aggradational cycles have been reported in the Cretaceous-Paleogene of West Texas (Atchley *et al.*, 2004), the Triassic of New Mexico (Cleveland *et al.*, 2007), and the Eocene of northern Wyoming (Kraus, 1987; Abels *et al.*, 2013). These cycles are meter-scale, with typically fining-upward successions. They generally consist of two phases: (1) an overbank phase with relative channel stability and strong paleosol development on fine clastic sediments; and (2) an avulsion phase characterized by channel instability and weak to no pedogenesis on heterolithic sandy avulsion-belt deposits (Abels *et al.*, 2013).

Most fluvial aggradational cycles are reported to be driven by base-level variations possibly in combination with upstream climatic or tectonic changes, but they may be fully autogenic in nature as well (Clyde & Kristensen, 2003). The floodplain aggradation cycles in the Eocene Bighorn Basin are not thought to be driven by base-level change (Foreman *et al.*, 2012). Instead, the cycles have been reported as autogenic previously (Clyde & Kristensen, 2003), while more recent evidence exemplifies them to be driven by precession-scale climate change with a duration of around 20 kyr (Kraus & Aslan, 1993; Abdul Aziz *et al.*, 2008; Abels *et al.*, 2013; van der Meulen *et al.*, 2020). The latter demonstration forms the basis for this research.

Previous Bighorn Basin Eocene studies have characterized and dated these cycles of different ages in various 1-D stratigraphic sections, including cycles in parallel sections separated by up to 8 kilometers (Abdul Aziz *et al.*, 2008; Abels *et al.*, 2013, 2016; Westerhold *et al.*, 2018; van der Meulen *et al.*, 2020). However, the full 3-D characteristics of these cycles have not been studied. Lateral consistency of allogenically-driven cycles is suggested in previous studies and expected in the case of external climate control as that would influence the whole basin at the same time. Local, autogenic processes are, however, expected to cause lateral and vertical variability on top of the regionally-consistent stratigraphy driven by external climate forcing. The spatial and temporal scales at which these local, autogenic processes interact with regional, allogenic processes remain unknown (Straub & Foreman, 2018). These can also not be derived from numerical modelling, as upscaling from model results is impossible if models could not be directly linked to field cases (Wang *et al.*, 2021). It thus remains challenging to disentangle the astronomical climate forcing from autogenic process in the fluvial stratigraphy.

Here, we, therefore, analyze the floodplain aggradation cycles in continuous outcrops of the lower Eocene Willwood Formation in the McCullough Peaks area of the northern Bighorn Basin, Wyoming, to reveal their spatial consistency and variability and to elucidate the spatial and temporal scales at which autogenic and allogenic controls interact and dominate. The objectives of this study are fivefold: (1) to investigate the traceability of floodplain aggradation cycles over a larger lateral distance; (2) to reveal the regionally-average vertical thicknesses and variability among individual cycles through the stratigraphy; (3) to characterize the lateral variability within each cycle; (4) to evaluate compensational stacking through temporally-successive cycles; and (5) to discuss the possible interacting pathway between allogenic and autogenic forcing.

2. GEOLOGICAL SETTING

The Bighorn Basin is a Laramide intermontane basin bounded by the western Beartooth Mountains, southwestern Washakie Range, eastern Bighorn Mountains, and the northeastern Pryor Mountains from Paleocene to Early Eocene (Fig. 1; Lillegraven & Ostresh, 1988). Its drainage was toward the north and northeast during the deposition of the Willwood Formation (Neasham & Vondra, 1972; Wang *et al.*, 2022). The Absaroka Range was formed by volcanic activity during the late early and middle Eocene (Fig. 1; Smedes & Prostka, 1972). The eastern margin of the basin has always been a relatively gentle slope (Yonkee & Weil, 2015). All the mountainous areas expressed before or during the early Eocene were indicated to be possible provenances (Neasham & Vondra, 1972; Kraus & Middleton, 1987; Owen *et al.*, 2019; Wang *et al.*, 2022). Faults in the Washakie range likely had influenced the development of the Willwood sedimentary sequences (Yonkee & Weil, 2015), while those on the Bighorn Basin side of the Bighorn Mountains were not expected to have large influences on the Willwood fluvial system (Wing & Bown, 1985; Wang *et al.*, 2022).

The Bighorn Basin hosts one of the best-studied terrestrial successions for fluvial cyclicity, with much research carried out on paleosols and river avulsion deposits (Neasham & Vondra, 1972; Bown & Kraus, 1981; Kraus & Aslan, 1993; Abels *et al.*, 2013; Foreman *et al.*, 2012; Owen *et al.*, 2017; and many others). Lower Eocene sediments exhibit regular alternations that have been related to the autogenic behavior that is intrinsic in a fluvial depositional system (Clyde & Christensen, 2003) and to allogenic forcing that is extrinsic (Kraus & Aslan, 1993; Abdul Aziz *et al.*, 2008; Abels *et al.*, 2013). The paleoenvironments and paleoclimates in the basin have been extensively studied from floral and faunal fossils (Gingerich, 2010). The mammal stratigraphy and data collections provide an accurate stratigraphy within the frame of the other stratigraphic controls such as magnetostratigraphy, chemostratigraphy, and tephrastratigraphy (Clyde *et al.*, 1994; Gingerich, 2010). Abel *et al.* (2013) compiled existing age controls for the calculation of McCullough Peaks sediment accumulation rates and estimated sedimentary cycle durations, which, together with their own data, produce a geometric mean accumulation rate of 0.329 m/kyr and an estimated cycle duration of 21.6 kyr (see their Table 1), which is consistent with modulation by the climatic precession cycle. This is the basis for this research. In other words, these cycles are viewed to be precession-driven in this study, and our scope is to characterize their character and geometry, instead of proving their orbital origin.

The McCullough Peaks study area is in the northwestern part of the Bighorn Basin (Fig. 1) and comprises an area of relatively large exposures of basinal sediments. The study interval here represents about 0.9 Myr of geological time straddling the interval in which the Eocene Thermal Maximum 2 (ETM2) and subsequent H2 events occur (Abels *et al.*, 2016). This is an estimation by cycle counting based on the previous findings that these cycles are precession-driven.

3. METHODOLOGY

3.1 Field survey

Stratigraphic sections were measured by digging 0.5-1 m wide and 0.5-1 m deep trenches down to the fresh rock in the McCullough Peaks area of the Bighorn Basin (Fig. 1). Field units were designated based on field estimation of grain size; matrix color; abundance, size, and color of mottling;

presence, abundance, and size of carbonate nodules; and abundance and size of slickensides. Hand sampling and field descriptions followed methods detailed in the Soil Survey Manual (Soil Survey Division Staff, 1993). Five long trenches were logged, with three reported in Abels *et al.* (2012, 2013, 2016) and two reported here (see Fig. 2 for their locations). Palaeocurrent directions were measured from dune-scale cross-stratification (mainly planar and trough cross-stratification) in channelized sandstone bodies.

3.2 UAV-based photogrammetry

Photographs were taken automatically every three seconds by a 20-megapixel camera mounted on a multirotor unmanned aerial vehicle (UAV; DJI Phantom 4 Pro). The UAV was flown parallel to the outcrop surface manually at a speed of 5-10 m/s to provide a 60% horizontal overlap between successive photos.

The final model includes 21144 photos taken on 34 flights (Fig. 2), and it covers a total area of ~10 km^2. The studied stratigraphic succession is ~300 m thick and dips at ~2° towards the south. Fifty-seven ground control points (GCPs) were placed (Fig. 2) and surveyed using an Emlid Reach GNSS receiver, hereinafter referred to as the rover. Accuracy of GCPs was improved by using the Post-Processed Kinematic (PPK) positioning technique which compares the rover-recorded GCP position to a second Emlid Reach GNSS receiver that acted as a stationary local base station. Both the rover and base station recorded raw GNSS measurements, which were then processed using the open-source GNSS post-processing package RTKLIB. The position of the base station was calibrated by collecting several hours of data and running the PPK solution against the nearest public Continuous Operating Reference Station (CORS) based in Fishtail, Montana (P722). The GCP positions were then determined with centimeter accuracy relative to the local base station.

Agisoft PhotoScan (Version 1.4.3, July 2018; current Metashape) was used to build the 3-D digital models using the structure from the motion multi-view stereo (SfM-MVS) photogrammetric method. A triangulated digital surface mesh was created, and the photos were draped onto the surface as the texture. Due to the large size of the area mapped, the complete photogrammetric image set was split into 42 model sections. For each section, a tiled model was generated, allowing the entire 3-D outcrop model to be imported into LIME (version 2.2.2; Buckley *et al.*, 2019) for visualization and interpretation.

3.3 Cycle boundary identification

Cycle boundary tops are placed in the photogrammetric models at the transition from reddish-to-purple soils to yellowish heterolithic deposits (Fig. S1). This position is different from the procedure by Abels *et al.* (2013) who put cycle boundaries at the top of the strongest soil development index (SDI) values, which often corresponds to the top of the reddest soil. Abels *et al.* (2013) based their findings on trenched sections in which more fresh rock was described. In contrast, the photogrammetric models in this study are of weathered surfaces and it was impossible to determine the strongest Soil Development Index values from these model images. To increase the consistency of the photogrammetric model interpretations in all cycles and between interpreters, we therefore traced the red to yellow transitions that left less doubt in most places. Local factors might hinder lateral tracing of cycle boundaries. These are occurrences of channel sandstone bodies, splitting or merging of soil horizons, recent debris and vegetation over the outcrops, and the occasional low resolution of the photogrammetric model. Some boundaries show relatively clear red/purple to yellow transitions in different parts of the model that, when connected, appeared to be at different stratigraphic levels with offsets of some decimeters to 1 or 2 meters. In most cases, consistency could subsequently be found, while in some cases, overbank to avulsion phase transition was subsequently placed at the stronger of the two transitions and traced that way laterally across the model.

The cycle boundaries defined in this study are found to be higher (0.6 m on average and up to 3.5 m for the seven cycles shown in Fig. S1) than that of Abels *et al.* (2013). These cycle boundaries can separate the overbank phase of the lower cycle from the avulsion phase of the upper cycle. As we consistently place the cycle boundaries at the same sedimentary transition, the final quantitative results will not be influenced. The photogrammetric model used in this study is going to be publicly shared on the platform of V3Geo (website: https://v3geo.com/).

3.4 Variogram analysis

The variogram is a function of variance over lag distance h, with larger variogram values corresponding to longer lag distances (Fig. S2). Here the lag distance refers to the separation between a pair of two data points. More detailed explanations about the principle and application workflow of variogram can be found in Supplementary Text S1 and Figure S2.

A variogram can be calculated as follows (Pyrcz & Deutsch, 2003):

$$\gamma(\mathrm{h}) = \frac{1}{2N(h)} \sum_{\alpha=1}^{N(h)} (z(u_\alpha) - z(u_\alpha + h))^2 \qquad (1)$$

where $\gamma(\mathrm{h})$ is a measure of dissimilarity between two data points over lag distance h; $N(h)$ is the number of data point pairs; u_α is a data point at location α in 2-D space; $u_\alpha + h$ is a data point separated from u_α by the distance h; $z(u_\alpha)$ is the numerical value at the data point u_α; and $z(u_\alpha + h)$ is the numerical value at the location $u_\alpha + h$.

Cycle thicknesses are measured on outcrop surfaces in the model every 20 meters, which could be impossible at some locations due to vegetation, low model resolution, and recent debris. These thickness measurements are then analyzed as a 2-D directional variogram using Python codes by Pyrcz

(2020). Variograms are calculated in six directions that separate 180° into six equal azimuth zones (e.g. 0°, 30°, 60°, 90°, 120°, and 150°) after observation of any statistical anisotropy in the variogram map. The lag distance is set as 100 m, with a lag tolerance of 50 m. The search strategy utilizes a wide azimuth tolerance (30°) and a large bandwidth (2 km) to reduce the nugget effect near the origin (Zhang *et al.*, 2005). In a directional variogram, a range is identified when the sill ($\gamma(\mathrm{h}) = 1$) is reached (Fig. S2). Within the range, the cycle thickness at one locality is stochastically related to that at another locality, which is referred to as the spatial continuity of the cycle thickness. Such continuity is expected to be the largest in the paleoflow direction according to Pyrcz & Deutsch (2014).

3.5 Compensational stacking analysis

3.5.1 Coefficient of variation

The coefficient of variation (CV) is defined as the ratio of the standard deviation over the mean, and thus a smaller CV indicates less variability. To investigate possibly-present compensational stacking, successive cycles are combined as stratigraphic assemblages (hereinafter referred to as assemblages) for CV calculation. For example, Cycles 1 and 2 can be combined as an assemblage to test how the combined thickness varies over the study area (Figure S3). To compare the varied thicknesses among different assemblages, we rescale the thickness for each assemblage by dividing the assemblage's thickness over its regional mean. In this way, the mean of each assemblage's thickness equals 1, and CV becomes exactly the same as the standard deviation. An example is showcased in Supplementary Text S2 and Figure S3. In this study, we artificially define that the assemblage is fully compensated when the CV value stops decreasing and stabilizes.

3.5.2 Compensational stacking index

The standard deviation of sedimentation/subsidence (σ_{ss}) (Wang *et al.*, 2011) can be used to characterize the compensational timescale:

$$\sigma_{ss}(T) = \left\{\int_0^L \left[\frac{r(T;x)}{\hat{r}(x)} - 1\right]^2 dL\right\}^{1/2} \tag{2}$$

where $r(T;x)$ is the average deposition rate at a horizontal coordinate of *x* during a time interval of *T*, *L* is the cross-basin length, and $\hat{r}(x)$ is the local long-term sedimentation (or subsidence) rate.

Empirically, σ_{ss} is expected to decrease as *T* increases, following a power-law trend (Equation 3, Straub *et al.*, 2009; Wang *et al.*, 2011):

$$\sigma_{ss} = a'T^{-\kappa} \tag{3}$$

where a' is a coefficient, and κ is termed the compensation index.

By reorganizing Equation 3, we can get:

$$\log(\sigma_{ss}) = \log(a') - \kappa * \log(T) \tag{4}$$

Therefore, the slope is $-\kappa$, and the intersection is $\log(a')$ for the relationship between $\log(T)$ and $\log(\sigma_{ss})$.

As intuitively illustrated in Straub & Wang (2013), there is a compensational timescale (Tc) (see Figure 3 of Wang et al., 2011 for example) that separates the stratigraphy partially influenced by autogenic forcing and the stratigraphy only influenced by allogenic forcing (See their Figure 2 in Straub & Wang, 2013). Beyond this compensational timescale, κ equals 1 and the stratigraphic stacking is purely compensational (Straub *et al.*, 2009). A step-by-step practical workflow to identify the compensational timescale is presented in Supplementary Text S3.

4. RESULTS

4.1 Floodplain aggradation cycle traceability and composite stratigraphy

A total of 44 cycles are identified throughout the studied ~300-m stratigraphy in the model, and their boundaries are well recognizable stratigraphically and traceable laterally (Fig. 3). The stratigraphy in which the 44 cycles are recognized starts 7 cycles below the base of the Deer Creek Amphitheater section of Abels *et al.* (2013) and ends at/above the top of the Upper Deer Creek section of Abels *et al.* (2012) and Creek Star Hill section of Abels *et al.* (2016). The lower 10 cycles and upper 11 cycles have limited lateral extents within the photogrammetric model. Most of the other cycles can be traced over a maximum distance of 4 km in the NE-SW direction and ~2.5 km in the SE-NW direction. A composite section that includes all of the 44 cycles is constructed by combining available trenched sections (DCA and UDC sections; Abels *et al.* 2012, 2016). We have extended the cycle labelling system of Abels *et al.* (2013) and Abels *et al.* (2012) rather than starting a new one (see Fig. 4A). Cycles P1 to P3 correspond to ETM2 and cycles P5 to P8 correspond to H2 (Abels *et al.* 2012, 2016; Fig. 1).

The composite stratigraphy with 44 floodplain aggradation cycles has a cumulative thickness of ~300 m (Fig. 4A), which is based on 1-D data and thus no regional averages of cycle thicknesses are included. The thickness of individual cycles ranges between 3.4 m and 12.5 m, with an average of 6.8 m, a standard deviation of 2.0 m, and a CV of 29% (Fig. 4B).

4.2 Lateral thickness variability of individual floodplain aggradation cycles

Owing to outcrop availability, detailed mapping is limited to seven cycles in the middle of the photogrammetric model, labelled as cycles H to N in the cycle labelling system. Individual thicknesses of these seven cycles range between 2 m and 18 m with a CV range of 17% to 28% (Fig. 5). Regionally average thicknesses of these seven cycles vary between 3.7 m (cycle K) and 9.7 m (cycle L). The average of all cycle thicknesses is 7.3 m with a standard deviation of 2.6 m (Fig. 5). These numbers are comparable to those calculated for all 44 cycles in the 1-D composite section (6.8 ± 2.0 m, Fig. 4B) and previously reported values (Abels *et al.*, 2013).

We make a total of 22 digital sections in the photogrammetric model, such as section 14 (S14) in Figure 3B. In these sections, the seven cycles studied in detail are complete and free of channelized sandstone bodies. The top of cycle N is flattened in all sections to form a horizontal level for the sake of easy illustration, as is shown in Figure 6, in which cycle thicknesses vary rapidly in the lateral direction, with a maximum of 4 m over a distance of 400 m.

Variograms are calculated for the seven cycles to indicate the correlativity of the cycle thickness at one specific location to that at another over a certain distance. The correlatable distance is on average 1.3 km in the long-range direction (see its definition in Section 3.4) and 0.6 km in the short-range direction (Fig. 7A and Table S1). The aspect ratio of the variogram ellipse varies between 1.4 to 5.3, with an average of 2.2 (Table S1). The long-range azimuth ranges between N 310° and N 080°, averaging N 001° (Fig. 7B and Table S1), which coincides with the average paleoflow direction measured in the dune-scale cross-beddings in the field (4° ± 24°; Fig. 7C; Wang *et al.*, 2022). Individual 1-D variograms show repetitive, non-monotonic features (e.g. Fig. 8B), which are referred to as "cyclicity" by Pyrcz & Deutsch (2003). Meanwhile, there are also non-monotonic variograms that don't present repetitive patterns (e.g. Fig. 8E), which, together with the above-mentioned cyclicity, are referred to as the hole effect (cf. Pyrcz & Deutsch, 2003).

4.3 Vertical floodplain aggradation cycle stacking

A locally thicker floodplain aggradation cycle seemingly tends to stack on a locally thinner cycle and vice versa. Examples are the thicker-than-average cycle L and the thinner-than-average cycle M in Section S18 of Figure 6.

To quantify this compensational stacking behaviour, two metrics are used. Following the workflow in Section 3.5.1, we calculate CV values of stratigraphic assemblages containing various amounts of cycles at 22 sections (Fig. 9). Assemblages containing two successive cycles have a smaller CV than those containing one cycle (23% versus 14%), with a reduction of 53% of the total CV reduction (numerically calculated as $\frac{23\% - 14\%}{23\% - 6\%}$). Assemblages containing three successive cycles have a further reduced CV by 76% to 10%. The CV does not decrease further after the assemblages contain 6 successive cycles, stabilizing at 6% and thus indicating full compensation according to our definition in Section 3.5.1.

For the second metric, we calculate σ_{ss} using the composite section shown in Figure 4A based on the method described in Section 3.5.2. The predicted full compensational timescale corresponds to 12 cycles (Fig. 9), although it has to be noted that this result is based on the 1-D dataset that has the floodplain aggradation cycle as the basic stratigraphic unit. The traditional application scenario of this method has 3-D data with annual (e.g. Wang et al., 2021) to decennial to centennial-scale (Straub *et al.*, 2009) resolution.

5. DISCUSSION

5.1 Floodplain aggradation cycles – Lateral and vertical consistency

Floodplain aggradation cycles are dominant features in many alluvial records (Kraus & Aslan, 1997; Abels *et al.*, 2013; Atchley *et al.*, 2013). They are related to (i) phase of river stability and true overbank deposition on which strong paleosols may develop and (ii) phase of regional-scale river avulsion causing deposition of the heterolithic avulsion belt on which weak or no soils develop (Kraus & Aslan, 1993; Abels *et al.*, 2013). In the Bighorn Basin, the floodplain aggradation cycles have been recently linked to precession-scale climate change (Kraus & Aslan, 1993; Abdul Aziz *et al.*, 2008; Abels *et al.*, 2013, 2016; van der Meulen *et al.*, 2020), which forms the basis for this study. In other words, this study doesn't aim to prove the allogenic nature of these cycles, but to describe their character and geometry.

At least six different stratigraphic sections of three different intervals of time in the central and northern Bighorn Basin have now revealed similarly-thick floodplain aggradation cycles of 7 to 8 meters (Abdul Aziz *et al.*, 2008, Abels *et al.*, 2013, 2016; Westerhold *et al.*, 2018; van der Meulen *et al.*, 2020). Previously, lateral consistency was demonstrated in two 1-D parallel sections spaced 7.5 km with correlations confirmed by carbon isotopes (van der Meulen *et al.*, 2020). One-to-one cycle correlation from our study area to the Gilmore Hill area over 15 km was suggested by Westerhold *et al.* (2018), which, however, could not be independently confirmed by stratigraphic constraints. Here, we demonstrate lateral consistency of individual cycles in a 10 km^2 area and a maximum lateral distance of 4 km approximately in paleoflow directions. We demonstrate floodplain aggradation cycles to be a consistent component of alluvial stratigraphy in the lower Eocene Willwood Formation with 44 successive cycles producing ~300 m of stratigraphy. The lateral consistency of individual floodplain aggradation cycles as well as the vertical continuity and stability of characters of these cycles in stratigraphy in this study are in line with previous studies instantiating the allogenic nature of these floodplain aggradation cycles (Abels *et al.*, 2013, 2016; van der Meulen *et al.*, 2020).

Longer-term aggradation rates depend on the accommodation space creation (Foreman & Straub, 2017), which, in the case of the Bighorn Basin where sea/lake-level variation is absent, is related to tectonic subsidence. A total of 44 floodplain aggradation cycles with an average thickness of 6.8 m driven by precession cycles with a duration of ca. 20 kyr in the early Eocene, results in long-term sedimentation rates and so subsidence rates of ~0.34 m/kyr. This is in line with previous age dating that result in rates of 0.29-0.39 m/kyr with a geometric mean of 0.33 m/kyr (Clyde *et al.*, 1994; Westerhold *et al.*, 2007; Stap *et al.*, 2009; Gingerich, 2010; Abels *et al.*, 2012, 2013). All age dating demonstrates that erosion is not a significant factor at >10^4 year time scales (Abels *et al.*, 2016). Lateral tracing of the floodplain aggradation cycles in the Deer Creek area of the McCullough Peaks did not reveal significant erosional events eroding part of or whole cycles. The study area of 10 km^2 may be too small for conclusive results concerning erosion, although current dating and correlations between the Deer Creek area and the Gilmore Hill area do not suggest major erosive phases either (D'Ambrosia *et al.*, 2017).

The average thickness of 44 stacked floodplain aggradation cycles in the 1-D section (6.8 m) and that of 7 successive cycles (cycles H to N) that are mapped in the whole 3-D space (7.3 m) are quite similar. However, 7 successive cycles (cycles H to N) mapped in detail show different thicknesses also when averaged over the entire study area. We think this can be because of four different reasons. First, the insolation received on the top of the earth's atmosphere is influenced by the interference of individual precession components (Berger *et al.*, 1992), which results in different amplitudes and frequencies of the insolation patterns and possibly consequently the different thicknesses of the corresponding sedimentary cycles. (Fig. 5). Second, we cannot yet know whether the spatial consistency and variability of floodplain aggradation cycles recorded in our study area (~10 km^2) is indeed a basin-scale representation. Thinner cycles may display thickening features outside the study area. We think the current size of the study area is large enough to deduce conclusions about lateral consistency and variability of the cycles, but it cannot be excluded that (slightly) different numbers pop up when larger areas are analyzed. As mentioned above, a one-to-one cycle correlation to the Gilmore Hill area, which is 15 km apart, is made by Westerhold *et al.* (2018). But the correlation is implemented in the form of 1-D columns, the intermediate part between these two areas is lack in data, and the correlation awaits further examination. Third, the defined cycle boundary is arbitrary, even though it is the most logical place for tracing in the photogrammetric models. The cycle boundary at a certain location depends on the local deposition and so on a combination of autogenic and allogenic processes. This does not produce a fixed phase relation between the identified cycle boundary and precession-scale climate change, and thus, the thickness of individual cycles, even if measured in a wide lateral area, has to be analyzed with care. Last but not the least, the thicknesses of these cycles are subjected to the inherent sedimentary dynamics of the fluvial system as well as the differentiated compaction and consolidation that results from the influence of the paleogeography caused by earlier cycles on later cycles. In other words, the eventual cycle thickness reflects the influences of both allogenic and autogenic factors.

The climatic pathway of how astronomical climate change drives floodplain aggradation cycles remains so far enigmatic (Abels *et al.*, 2013) and needs further study. The pathway of astronomical cycles ultimately driving sedimentary change passes a series of intermediate steps that are not straightforward to predict. The first question is how astronomical cycles result in climate change, the second question is how climate change via which teleconnections result in changes in the depositional environment, and the last question is how changes in the depositional environment cause changes in stratigraphy. We refer here to the discussion on the climatic origin behind the cyclicity in Abels *et al.* (2013) and Wang *et al.* (2021). The final answer behind the origin of the precession-forcing of the floodplain aggradation cycles should lie in an interplay between changes in water discharge hydrograph, sediment discharge, and catchment and basinal vegetation, together with the gradual build-up of superelevation at pace with such cyclic climatic changes in order that these trigger regional-scale avulsion followed by a renewed 'overbank phase' (Abels *et al.*, 2013; Wang *et al.*, 2021).

5.2 Floodplain aggradation cycles – Lateral variability

Thicknesses of individual floodplain aggradation cycles may change rapidly in the lateral direction with a maximum changing rate of up to 4 m over a lateral distance of 400 m (Fig. 6). It should be noted that all of the geometries discussed here are derived from compacted stratigraphy. Part of the variability that is measured likely relates to differential compaction between different lithologies. We did attempt to decompact the series and reconstruct these differential thicknesses but we were so far unsuccessful, as we found out this requires detailed information on early-stage consolidation and later-stage compaction and the exact rates of these. Differential, early-stage consolidation may cause higher or lower sedimentation in different areas (Toorman, 1999) and thus influence the subsequent thicknesses of stratigraphy, while late-stage compaction does not impact sedimentation (Terzaghi & Peck, 1968). We envision that a dynamic backstripping exercise with active sedimentation and thus knowledge about rates of sedimentation depending on topography is needed to decompact the succession and reconstruct the paleotopography (Celerier, 1988). That is clearly beyond the scope of the current work. Therefore, all the results we present and discuss are of compacted stratigraphy. It is thus also not yet possible to calculate floodplain roughness and topographic differences in the early Eocene fluvial landscape of the Bighorn Basin.

The lateral thickness variability of all the seven cycles mapped in detail within the 10 km^2 study area is attributed here to morphologic variability within the fluvial system in combination with differential compaction as discussed above. Morphologic elements in the fluvial landscape are major and minor channel belts, crevasse splays, levees, and floodplains. These caused different rates and types of sedimentation in different areas, which thereby resulted in topographic gradients between them (Hajek & Straub, 2017). Thicker-than-average cycles at some localities are more often dominated by crevasse splay sediments (Figure 3B), and their overlying sediments are finer and more often dominated by distal floodplain soils. Thick, sandy crevasse splays thus seem to concentrate in apparently low-lying areas where clay-rich, strongly pedogenic overbank deposits were deposited before.

The spatial continuity of the cycle thicknesses is stronger in the direction of paleoflow than perpendicular to paleoflow (Fig. 7). This could be indicative of how floodplain deposits are morphologically segmented by channel belts oriented in the downstream direction. Floodplain segmentation could depend on the number of river threads active at the same time or in the same stratigraphic interval and on the frequency and magnitude of river flooding and crevasse splaying. Correlation between cycle thickness at one locality and that at another locality does not decrease continuously with the increasing lag distance (Fig. 8). Instead, increasing lag distance may be associated with increasing correlation (and decreasing variogram values), showing the co-called cyclicity in the variogram results (see Pyrcz & Deutsch, 2003). This increasing correlation at larger distances could mean that similar floodplain characteristics come back after an initial distance at which correlation was poor. This could point to the size of morphological elements in the fluvial landscape. In our field data, the variogram analysis reveals such elements to re-occur at km-scale (Fig. 8). However, first, we think the study area is too small compared to the expected size of elements in the fluvial landscape, particularly when major channel belts are to be included in the analysis. And, second, the analysis is done on compacted series, and decompacted stratigraphy may give us (slightly) different results.

We analyze, using similar methods, the numerically-modelled stratigraphy of Wang *et al.* (2021). In their Scenario A40, water discharge and sediment input are fed cyclically with a wavelength of 10 kyr and an amplitude of 40%, which produces four cycles that mimic those in the Bighorn Basin. Variogram analysis is implemented using the thickness map of the third floodplain aggradation cycle in the center of the basin to avoid the too strong impact of either upstream or downstream factors (Fig. 10). Interestingly, we find a long range of 22 km in the direction of paleoflow and a short range of 6 km perpendicular to paleoflow in the cross-basin direction (Fig. 10D). Increasing correlations with increasing lag distances, the so-called hole effect and variogram cyclicity, are also observed in the modeled data (azimuth N 030°, Fig. 10D). Strong correlation (low variogram values) comes back at distances above 10 km (azimuth N 030°, Figure 10D) and seems to relate to sizes of major channel belts

(Fig. 10A to C). The topographic lows and highs caused by channel belts and nearby coarse sediment deposition are expected to result in the segmentation of floodplain fines.

5.3 Compensational stacking of floodplain sedimentation

Compensational stacking refers to the tendency of a depositional system to fill the lows and erode the highs in topography (Straub *et al.*, 2009; Straub & Pyles, 2012). In other words, relatively high or low topography in the local areas of the paleogeography will lead to local higher deposition or erosion rates during the formation of subsequent and overlying floodplain aggradation cycles. Therefore, compensational stacking is expected to significantly reduce the topographic differences if the depositional time is sufficiently long, which means the smoothing effect of the later deposited cycle is much larger than the newly introduced morphological variability. Several other factors are also influential, in particular the early consolidation effect that may result in variable topography that was originally relatively flat. For example, sandstone bodies remain high in the landscape as these consolidate less, while floodplain clay or even peat eventually produce lows in the landscape as these relatively consolidate more. Therefore, we attribute the compensational stacking found in this study to be the result of both fluvial morphology and compaction. In section 5.2, we have discussed why decompaction at these scales has been unfeasible within the current study.

Two metrics (i.e., CV and σ_{ss}) point to full compensational timescales corresponding to 6 and 12 floodplain aggradation cycles (*ca* 120-240 kyr), respectively. However, 54% compensational stacking is already reached in the subsequent first cycle and 76% in the subsequent two cycles in the CV dataset. The remaining 23% compensational stacking occurs when the stacked cycle number increases from 3 to 6 in which CV drops from 9% to 6%. Full compensational timescales obtained based on these two metrics are different because they are based on different methods applied to different datasets. The CV metric is based on measurements of the lateral thickness data of seven cycles in 22 digital sections over the whole study area (data from Figure 6 and results shown in Figure 9), whereas the compensational index method is based on a long 1-D composite section (data from Figure 4 and results shown in Figure 9) lacking lateral data. The CV metric is favored because of the underlying 3-D dataset, but it comprises a limited stratigraphic interval. The compensational index method is based on a very long sedimentary record (~300 m), but it is applied in a 1-D dataset instead of a 3-D one. Therefore, the compensational timescales we obtain here await examination by both spatially wider and stratigraphically longer datasets. We expect that the compensational timescale will be reached in a much shorter time in a 3-D dataset, which is, however, unavailable in this study due to outcropping limitations.

The calculated full compensational timescales up to 120 or 240 kyr are longer than those identified in previous research. In a fully autogenic numerical scenario by Wang *et al.* (2021), a compensational time scale of only 2000 years in the modelling domain was calculated. Straub *et al.* (2020) calculated 67 kyr, 100 kyr, and 55 kyr compensational timescales based on the estimation of the maximum channel belt sandstone body thickness and the long-term sedimentation rate respectively in the Bighorn Basin, Piceance Creek Basin, and Tremp-Graus Basin. The major part of the compensation occurs in our case at 20 to 40 kyr. The 67 kyr calculate by Straub et al. (2020) thus lies in the middle between the major compensation timescale (20 to 40 kyr) and the full compensation timescale we calculate (120 to 240 kyr). Straub & Pyles (2012) state that units as small as individual channel beds are compensating for the topographic differences created by older beds, whereas units of channel stories and higher hierarchy (i.e. channel element and channel complex) are also compensating one another during their stacking. One certain thing is that the full compensational timescale we calculate here is not the autogenic timescale (cf. Powell *et al.*, 2012; Foreman & Straub, 2018; Straub *et al.*, 2020) because the basic stratigraphic unit we use is more allogenic in nature (20 kyr). Increasing time-resolution in our field case is not the scope of this study and also very difficult as age constraints lack to trace time stratigraphic lines below the 20 kyr time scales in these series.

Paleogeography of the fluvial landscape is partly reflected by the cycle thickness variability we discuss in 5.2, while it is also partly represented by the paleochannel features, and a larger paleochannel depth corresponds to a longer autogenic timescale in the precondition that there are no significant interferences from allogenic forcing. The thickest sandstone body in the study area is 23 m (see Figure 5.3, Wang, 2021), while the geometric mean accumulation rate is 0.329 m/kyr (see Table 1, Abels et al., 2013). Therefore, the autogenic timescale would be 70 kyr according to the estimation method of Straub *et al.* (2020), which is very close to the estimation of 67 kyr by Straub *et al.* (2020). The compensational timescale (different from the autogenic timescale when strong allogenic forcing is present) is demonstrated to be prolonged by 2.5 times from 2.0 kyr to 5.1 kyr when there is allogenic forcing in the numerical model (see Figure 4 of Wang *et al.*, 2020). Therefore, we expect the true compensational timescale to be a value between 70 and 240 kyr, when sufficiently long records with sufficient regional coverage is available. Our study provides insights into the compensational stacking of geological bodies over a higher hierarchy, similar to results by Straub & Pyles (2012), while also exemplifying a sensitivity analysis of this method when using datasets different from traditional ones.

5.4 Disentangling autogenic and allogenic drivers of floodplain sedimentation

One of the goals of this study has been to disentangle the allogenic from autogenic sedimentation scales in the alluvial succession of the Bighorn Basin. The laterally-consistent floodplain aggradation cycles are in line with previous studies demonstrating their allogenic, cyclic forcing. Local, autogenic processes relate to variable crevasse splaying, local avulsions and minor distributaries, compensationally stacking fluvial topography and producing an interplay with the externally-driven, consistent floodplain aggradation cycles. The very stable average thickness of these floodplain aggradation cycles relates to the external forcing where net subsidence rates are at pace with climate cycle deposition. The variability of the thickness of the floodplain aggradation cycles in a lateral sense is driven by autogenic dynamics. The smaller standard deviation (4.0-5.2 m) than the average cycle thickness (7.0 m) would allow us to disentangle allogenic from autogenic forcing in the series qualitatively and quantitatively as some of the spatial and temporal impacts of both allogenic and autogenic controls have been quantified here. In other words, for the compacted floodplain stratigraphy in this study, the measured vertical scales of autogenic processes are 4.0 to 5.2 m at the 95% significance level depending on whether the data are from the regionally-mapped seven successive cycles (Fig. 5) or the 44 successive cycles throughout a thick composite stratigraphy (Fig. 4). These numbers are below the scales of precession-climate drivers occurring at 6.8 to 7.3 m thickness, which is probably why autogenic and allogenic drivers can be disentangled in this series. The above analysis is for floodplain stratigraphy, and it is expected that major channel belts could result in larger vertical autogenic scales.

The study area of 10 km^2 may not be sufficiently large compared to the basin size or compared to the scales at which the fluvial systems act and interact in the fluvial landscapes over time. Autogenic factors may eventually generate similar products to those generated by allogenic factors, even at large scales such as those of our study area. For the current study, the area could not have been larger, even though enlargement seems still possible towards the Gilmore Hill area of the McCullough Peaks and tentative cycle-to-cycle correlations have been made by Westerhold *et al.* (2018). To the west, low angle faults prevent the enlargement of the study area, while areas to the north and south of the study area are in lack of outcrops of the same stratigraphic interval. We hope our study provides certain insights to workers in the other sedimentary basins where a larger study area is available.

The specific size of the morphological elements in this fluvial system will determine the spatial scale of autogenic variability in the rock record together with the activity of these elements (Hajek *et al.*, 2012; Straub & Foreman, 2018). The dominance of this autogenic variability in the stratigraphic record is in part largely determined by the aggradation rates. High aggradation rates will cause the imprints of autogenic variability to be spread through the record and of a relatively smaller scale compared to the allogenic climate forcing. Low aggradation rates will cause single levels to be dominated by autogenic variability and allogenic climate forcing to be blurred in stratigraphy (Straub & Foreman, 2018; Wang *et al.*, 2021). As such, floodplain aggradation cycles will be less visible in those low-aggradation settings compared to high-aggradation settings, which is similar when it comes to the effect of the allogenic signal wavelength (Wang et al., 2021). However, to what extent autogenic processes may act also at these longer timescales, particularly when allogenic triggers are absent, remains enigmatic and needs further research.

6. CONCLUSIONS

Analysis of a 3-D photogrammetric model covering an area of ~10 km^2 and a succession thickness of ~300 m in the McCullough Peaks Area of the Bighorn Basin reveals a total of 44 stacked floodplain aggradation cycles, with an average thickness of 6.8 m and a standard deviation of 2.0 m. We find a strong lateral consistency of the floodplain aggradation cycles over the entire photogrammetric model and a solid continuity in stratigraphy in line with previous studies that suggest the occurrence of these cycles at precession-time scales. Meanwhile, these floodplain aggradation cycles display a strong lateral thickness variability that is ascribed to autogenic processes in the fluvial system. Cycle thickness may change as rapidly as 1 m over 100 m when traced laterally, with a maximum of 4 m. Variogram analysis shows that the thickness of an individual cycle at a specific locality is related to that at another locality over an average distance of 1.3 km in the paleoflow direction and 0.6 km perpendicular to the paleoflow direction. We attribute this to the more continuous fluvial morphodynamic elements in paleoflow directions. Compensational stacking of floodplain aggradation cycles is observed mostly at scales of 40-60 kyr, while full compensation seems to occur after 120-240 kyr. In compacted floodplain stratigraphy, the measured vertical scale of autogenic processes impacting stratigraphy is 4.0 to 5.2 m at 95% significance. This is below the scales of precession-climate drivers occurring at around 7.0 m thickness, which is probably why autogenic and allogenic drivers can be disentangled in this series.

ACKNOWLEDGEMENTS

This study was financially supported by Top Sectors GeoEnergie, Equinor, and Wintershall to HAA, JEAS, AWM, and TFB (FRESCO Project, Grant No. TKI2018–03–GE), a China Scholarship Council grant to YW (No. 201606440046), the Dutch Molengraaff fund to YW (Stichting Molengraaff Fonds), and the IAS/SEPM travel grants to YW that indirectly contributes to the 2019 field visit. The authors acknowledge the help from Chaowen Wang, Dirk-Jan Walstra, Hiranya Sahoo, and the Churchill family of Wyoming for help and encouragement in the field, Jasper de Lanoy for the earlier photogrammetric model interpretations, and Suihong Song for discussion on variogram analysis. We thank the Ph.D. committee members of YW for their suggestions on the chapter that is converted to the original manuscript, including Dr. Chris Fielding, Dr. Giovanni Bertotti, Dr. Gary Hampson, and Dr. Klaudia Kuiper, as well as reviewers and editors of *EPSL* including Dr. Sébastian Carretier, an anonymous reviewer, and chief editor Dr. Jean-Philippe Avouac for thoughtful and helpful reviews that allowed us to improve an earlier version of our manuscript.

REFERENCES

Abdul Aziz, H., **Hilgen, F.J.**, **van Luijk, G.M.**, **Sluijs, A.**, **Kraus, M.J.**, **Pares, J.M.** and **Gingerich, P.D.** (2008) Astronomical climate control on paleosol stacking patterns in the upper Paleocene–lower Eocene Willwood Formation, Bighorn Basin, Wyoming. *Geology*, **36**, 531–534.

Abels, H.A., **Clyde, W.C.**, **Gingerich, P.D.**, **Hilgen, F.J.**, **Fricke, H.C.**, **Bowen, G.J.** and **Lourens, L.J.** (2012) Terrestrial carbon isotope excursions and biotic change during Palaeogene hyperthermals. *Nat. Geosci.*, **5**, 326–329.

Abels, H.A., **Kraus, M.J.** and **Gingerich, P.D.** (2013) Precession-scale cyclicity in the fluvial lower Eocene Willwood Formation of the Bighorn Basin, Wyoming (USA). *Sedimentology*, **60**, 1467–1483.

Abels, H.A., **Lauretano, V.**, **van Yperen, A.E.**, **Hopman, T.**, **Zachos, J.C.**, **Lourens, L.J.**, **Gingerich, P.D.** and **Bowen, G.J.** (2016) Environmental impact and magnitude of paleosol carbonate carbon isotope excursions marking five early Eocene hyperthermals in the Bighorn Basin, Wyoming. *Clim. Past*, **12**, 1151–1163.

Allen, J.R.L. (1978) Studies in fluviatile sedimentation: an exploratory quantitative model for the architecture of avulsion-controlled alluvial suites. *Sediment. Geol.*, **21**, 129–147.

Atchley, S.C., **Nordt, L.C.** and **Dworkin, S.I.** (2004) Eustatic Control on Alluvial Sequence Stratigraphy: A Possible Example from the Cretaceous-Tertiary Transition of the Tornillo Basin, Big Bend National Park, West Texas, U.S.A. *J. Sediment. Res.*, **74**, 391–404.

Berger, A., **Loutre, M.F.** and **Laskar, J.** (1992) Stability of the Astronomical Frequencies Over the Earth’s History for Paleoclimate Studies. *Science*, **255**, 560–566.

Birgenheier, L., **Vanden Berg, M.**, **Plink-Bjorklund, P.**, **Gall, R.**, **Rosencrans, E.**, **Rosenberg, M.J.**, **Toms, L.C.** and **Morris, J.** (2019) Climate impact on fluvial-lake system evolution, Eocene Green River Formation, Uinta Basin, Utah, USA. GSA Bull. Doi: 10.1130/B31808.1

Bridge, J.S. and **Leeder, M.R.** (1979) A simulation model of alluvial stratigraphy. *Sedimentology*, **26**, 617–644.

Buckley, S.J., **Ringdal, K.**, **Naumann, N.**, **Dolva, B.**, **Kurz, T.H.**, **Howell, J.A.** and **Dewez, T.J.B.** (2019) LIME: Software for 3-D visualization, interpretation, and communication of virtual geoscience models. *Geosphere*, **15**, 222–235.

Cleveland, D.M., **Atchley, S.C.** and **Nordt, L.C.** (2007) Continental Sequence Stratigraphy of the Upper Triassic (Norian Rhaetian) Chinle Strata, Northern New Mexico, U.S.A.: Allocyclic and Autocyclic Origins of Paleosol-Bearing Alluvial Successions. *J. Sediment. Res.*, **77**, 909–924.

Clyde, W., **Stamatakos, J.** and **Gingerich, P.** (1994) Chronology of the Wasatchian Land-Mammal Age (Early Eocene): Magnetostratigraphic Results from the McCullough Peaks Section, Northern Bighorn Basin, Wyoming. J Geol. doi: 10.1086/629680

Clyde, W.C. and **Christensen** (2003) Testing the relationship between pedofacies and avulsion using Markov analysis. *Am. J. Sci.*, **303**, 60–71.

D'Ambrosia, A.R., **Clyde, W.C.**, **Fricke, H.C.**, **Gingerich, P.D.** and **Abels, H.A.** (2017) Repetitive mammalian dwarfing during ancient greenhouse warming events. *Sci. Adv.*, **3**, e1601430.

Finn, T.M., Kirschbaum, M.A., Roberts , S.B., Condon, S.M., Roberts, L.N.R.,and Johnson, R.C. (2010) Cretaceous–Tertiary Composite Total Petroleum System (503402), Bighorn Basin, Wyoming and Montana, *U.S. Geological Survey Digital Data Series DDS-69-V*, 157 p.

Foreman, B.Z., **Heller, P.L.** and **Clementz, M.T.** (2012) Fluvial response to abrupt global warming at the Palaeocene/Eocene boundary. *Nature*, **491**, 92–95.

Foreman, B. Z. & **Straub, K. M.** (2017) Autogenic geomorphic processes determine the resolution and fidelity of terrestrial paleoclimaterecords. *Science Advances*, 3(9), e1700683.

Gingerich, P. D. (2010) Mammalian faunal succession through the Paleocene-Eocene thermal maximum (PETM) in western North America. *Vertebrata PalAsiatica*, **48**, 308–327**.**

Hajek, E.A. and **Straub, K.M.** (2017) Autogenic Sedimentation in Clastic Stratigraphy. *Annu. Rev. Earth Planet. Sci.*, **45**, 681–709.

Hajek, E.A. and **Wolinsky, M.A.** (2012) Simplified process modeling of river avulsion and alluvial architecture: Connecting models and field data. *Sediment. Geol.*, **257–260**, 1–30.

Karssenberg, D. and **Bridge, J.S.** (2008) A three-dimensional numerical model of sediment transport, erosion and deposition within a network of channel belts, floodplain and hill slope: extrinsic and intrinsic controls on floodplain dynamics and alluvial architecture. *Sedimentology*, **55**, 1717–1745.

Kraus, M.J. (1987) Integration of channel and floodplain suites, II. Vertical relations of alluvial paleosols. *J. Sed. Petrol.*, **57**, 602–612.

Kraus, M.J. and **Aslan, A.** (1993) Eocene hydromorphic paleosols: significance for interpreting ancient floodplain processes. SEPM J Sediment Res. Doi: 10.1306/D4267B22-2B26-11D7-8648000102C1865D

Kraus, M.J. and Middleton, L. (1987) Contrasting architecture of two alluvial suites in different structural settings. In: F.G. Ethridge, R.M. Fiores and M.D. Harvey (Editors). *Recent Developments in Fluvial Sedimentology. SEPM Spec. Pubi.*, **39**, 253-262.

Lillegraven, J.A. and **Ostresh, L.M., Jr.** (1988) Evolution of Wyoming's early Cenozoic topography and drainage patterns: National Geographic Research, **4**, p. 303–327.

Mohrig, D., **Heller, P.L.**, **Paola, C.** and **Lyons, W.J.** (2000) Interpreting avulsion process from ancient alluvial sequences: Guadalope-Matarranya system (northern Spain) and Wasatch Formation (western Colorado). *Geol. Soc. Am. Bull.*, 17.

Neasham, J.W. and **Vondra, C.F.** (1972) Stratigraphy and Petrology of the Lower Eocene Willwood Formation, Bighorn Basin, Wyoming. *Geol. Soc. Am. Bull.*, **83**, 2167.

Owen, A., **Ebinghaus, A.**, **Hartley, A.J.**, **Santos, M.G.M.** and **Weissmann, G.S.** (2017) Multi-scale classification of fluvial architecture: An example from the Palaeocene-Eocene Bighorn Basin, Wyoming. *Sedimentology*, **64**, 1572–1596.

Powell, E.J., Kim, W., and **Muto, T.** (2012) Varying discharge controls on timescales of autogenic storage and release processes in fluvio-deltaic environments: Tank experiments. *J. Geophys. Res. Earth Surf.*, **117**, F02011.

Pyrcz, M. (2020). GitHub repository, https://github.com/GeostatsGuy/

Pyrcz, M. and **Deutsch, C. V.** (2003) The whole story on the hole effect. *Geostatistical Association of Australasia, Newsletter*, **18**.

Pyrcz, M. and **Deutsch, C.V.** (2014) Geostatistical reservoir modeling, Second edition. *New York, New York : Oxford University Press*, Oxford, 433 pp.

Slingerland, R. and **Smith, N.D.** (2004) RIVER AVULSIONS AND THEIR DEPOSITS. *Annu. Rev. Earth Planet. Sci.*, **32**, 257–285.

Soil Survey Division Staff (1993) Soil Survey Manual, vol. 18. Soil Conservation Service, U.S. Department of Agriculture, USA.

Smedes, H.W. and **Prostka, H.J.** (1972) Stratigraphic framework of the Absaroka Volcanic Supergroup in the Yellowstone National Park region. *U.S. Geological Survey Professional Paper*, 729-C, 33 p.

Stap, L., **Sluijs, A.**, **Thomas, E.** and **Lourens, L.** (2009) Patterns and magnitude of deep sea carbonate dissolution during Eocene Thermal Maximum 2 and H2, Walvis Ridge, southeastern Atlantic Ocean. Paleoceanography. doi: https://doi.org/10.1029/2008PA001655

Straub, K.M., **Duller, R.A.**, **Foreman, B.Z.** and **Hajek, E.A.** (2020) Buffered, Incomplete, and Shredded: The Challenges of Reading an Imperfect Stratigraphic Record. J Geophys Res Earth Surf. doi: 10.1029/2019JF005079

Straub, K.M. and **Foreman, B.Z.** (2018) Geomorphic stasis and spatiotemporal scales of stratigraphic completeness. *Geology*, **46**, 311–314.

Straub, K. M. and **Wang, Y.** (2013). Influence of water and sediment supply on the long-term evolution of alluvial fans and deltas: Statistical characterization of basin-filling sedimentation patterns. *Journal of Geophysical Research: Earth Surface*, **118**, 1– 15.

Straub, K.M., **Paola, C.**, **Mohrig, D.**, **Wolinsky, M.A.** and **George, T.** (2009) Compensational Stacking of Channelized Sedimentary Deposits. *J. Sediment. Res.*, **79**, 673–688.

Straub, K.M. and **Pyles, D.R.** (2012) Quantifying the Hierarchical Organization of Compensation In Submarine Fans Using Surface Statistics. *J. Sediment. Res.*, **82**, 889–898.

Toorman E.A. (1996) Sedimentation and self-weight consolidation: general unifying theory. *Geotechnique*, 46(1):103–113

van der Meulen, B., **Gingerich, P.D.**, **Lourens, L.J.**, **Meijer, N.**, **van Broekhuizen, S.**, **van Ginneken, S.** and **Abels, H.A.** (2020) Carbon isotope and mammal recovery from extreme greenhouse warming at the Paleocene–Eocene boundary in astronomically-calibrated fluvial strata, Bighorn Basin, Wyoming, USA. *Earth Planet. Sci. Lett.*, **534**, 116044.

Wang, Y. (2021) Alluvial Stratigraphic Response to Astronomical Climate Change: Numerical modelling and outcrop study in the Bighorn Basin, Wyoming, USA. PhD thesis, TU Delft.

Wang, C., **Adriaens, R.**, **Hong, H.**, **Elsen, J.**, **Vandenberghe, N.**, **Lourens, L.J.**, **Gingerich, P.D.** and **Abels, H.A.** (2017) Clay mineralogical constraints on weathering in response to early Eocene hyperthermal events in the Bighorn Basin, Wyoming (Western Interior, USA). *Geol. Soc. Am. Bull.*, **129**, 997–1011.

Wang, Y., Baars, T.F., Sahoo, H., Storms, J.E.A., Martinius, A.W., Gingerich, P.D., and **Abels, H.A.** (2022). Sandstone body character and river planform styles of the lower Eocene Willwood Formation, Bighorn Basin, Wyoming, USA. *Sedimentology*, in press. Doi: https://doi.org/10.1111/sed.13027

Wang, Y., **Storms, J.E.A.**, **Martinius, A.W.**, **Karssenberg, D.** and **Abels, H.A.** (2020) Evaluating alluvial stratigraphic response to cyclic and non-cyclic upstream forcing through process-based alluvial architecture modelling. *Basin Res.*, **33**, 48–65.

Wang, Y., **Storms, J.E.A.**, **Martinius, A.W.**, **Karssenberg, D.** and **Abels, H.A.** (2021) Evaluating alluvial stratigraphic response to cyclic and non-cyclic upstream forcing through process-based alluvial architecture modelling. *Basin Res.*, **33**, 48–65.

Wang, Y., **Straub, K.M.** and **Hajek, E.A.** (2011) Scale-dependent compensational stacking: An estimate of autogenic time scales in channelized sedimentary deposits. *Geology*, **39**, 811–814.

Westerhold, T., **Röhl, U.**, **Laskar, J.**, **Raffi, I.**, **Bowles, J.**, **Lourens, L.J.** and **Zachos, J.C.** (2007) On the duration of magnetochrons C24r and C25n and the timing of early Eocene global warming events: Implications from the Ocean Drilling Program Leg 208 Walvis Ridge depth transect. Paleoceanography. Doi: https://doi.org/10.1029/2006PA001322

Westerhold, T., **Röhl, U.**, **Wilkens, R.H.**, **Gingerich, P.D.**, **Clyde, W.C.**, **Wing, S.L.**, **Bowen, G.J.** and **Kraus, M.J.** (2018) Synchronizing early Eocene deep-sea and continental records – cyclostratigraphic age models for the Bighorn Basin Coring Project drill cores. *Clim. Past*, **14**, 303–319.

Wing, S. and **Bown, T.M.** (1985) Fine Scale Reconstruction of Late Paleocene-Early Eocene Paleogeography in the Bighorn Basin of Northern Wyoming. In Flores, R., and Kaplan, S., eds., Cenozoic paleogeography of the west-central United States: Rocky Mountain Section, *Society of Economic Paleontologists and Mineralogists*, pp. 93–105.

Yonkee, W.A. and **Weil, A.B.** (2015) Tectonic evolution of the Sevier and Laramide belts within the North American Cordillera orogenic system. *Earth-Science Reviews*, **150**, 531–593.

Zhang, Y., **Person, M.**, **Paola, C.**, **Gable, C.W.**, **Wen, X.-H.** and **Davis, J.M.** (2005) Geostatistical analysis of an experimental stratigraphy: geostatistical analysis of experimental stratigraphy. Water Resour Res. doi: 10.1029/2004WR003756

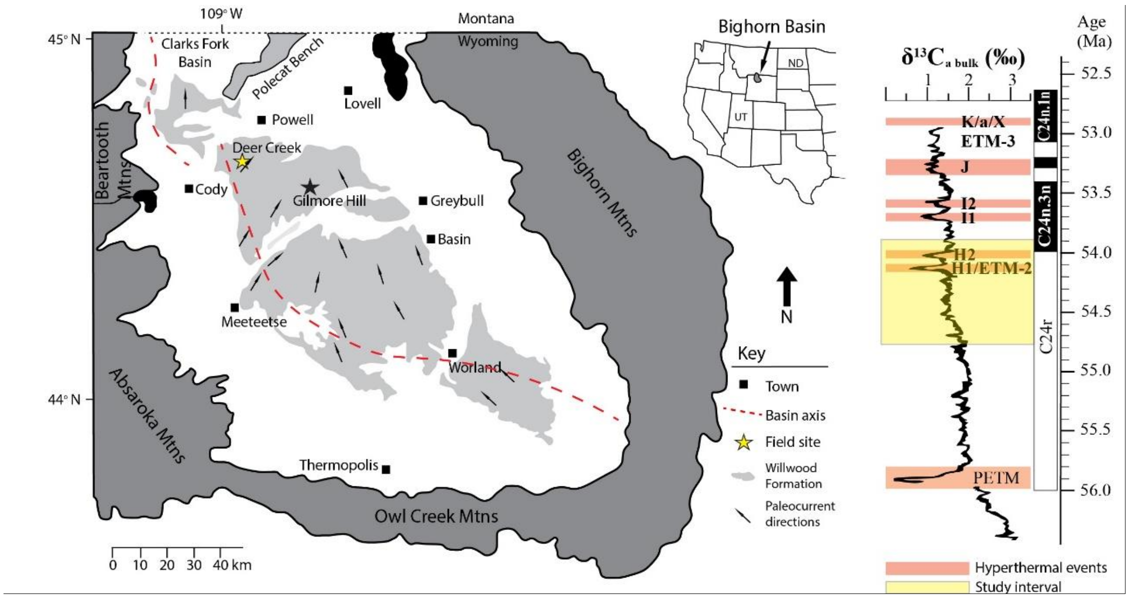

Figure 1. The left panel shows the location of the study area, the McCullough Peaks, in the northern Bighorn Basin, Wyoming (modified after Wang *et al.*, 2018), with the paleoflow direction provided by Neasham and Vondra (1972) and the basin axis following Finn et al. (2010). The right stratigraphic column shows the rough stratigraphic position of the study interval, of which upper and lower boundaries are estimated by calculating the amount of sedimentary cycles above and below ETM-2 based on previous studies that attribute these cycles to be precession-driven (Abels *et al.*, 2013; Westerhold *et al.*, 2018). The δ^{13}Ca bulk data are adjusted from Zachos et al. (2010) to Gradstein et al. (2012) global timescale (Vandenberghe et al., 2012) by Birgenheier *et al.* (2019). Existing age control for stratigraphic intervals close to ours can be found in table 1 of Abels et al. (2013).

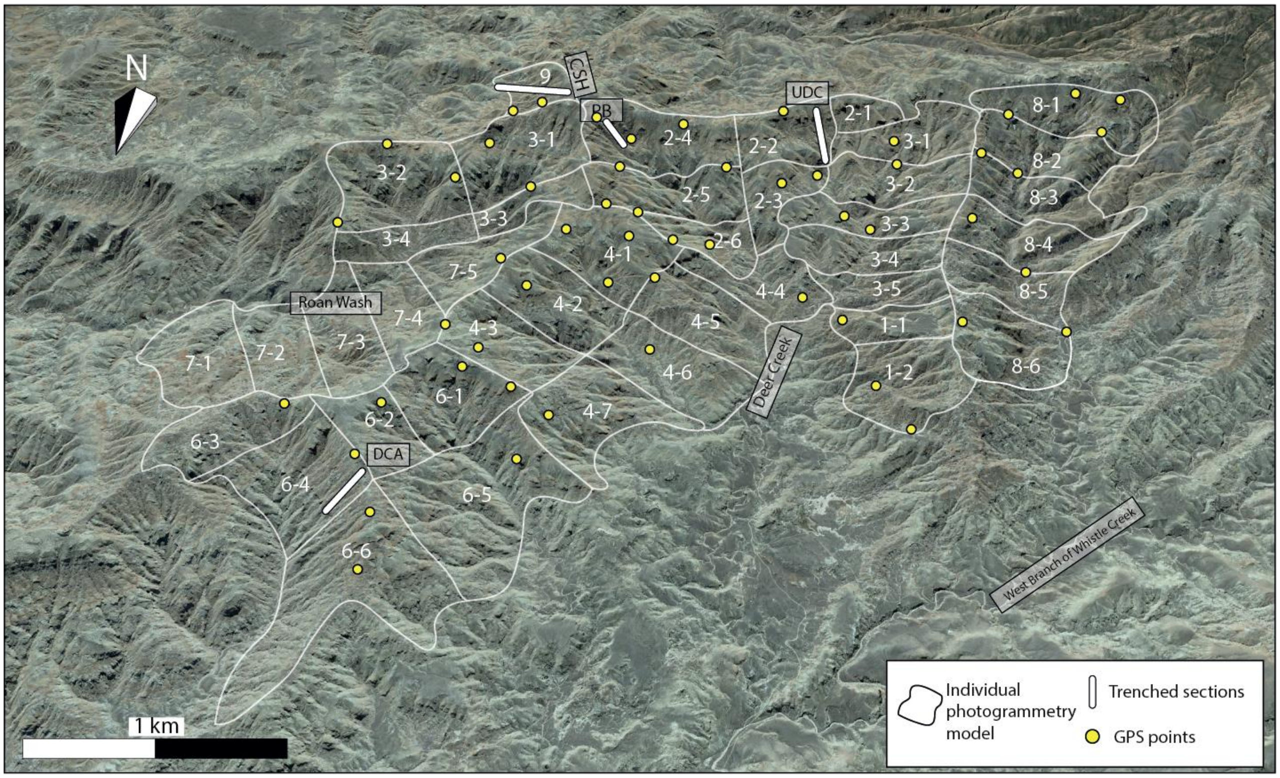

Figure 2. A bird's eye view from Google Earth showing the coverage of 42 individual photogrammetric 3-D models. Abbreviations: DCA--Deer Creek Amphitheater section (Abels *et al.*, 2013), PB--Purple Butte section, UDC--Upper Deer Creek section (Abels *et al.*, 2012), and CSH--Creek Star Hill section (Abels *et al.*, 2016).

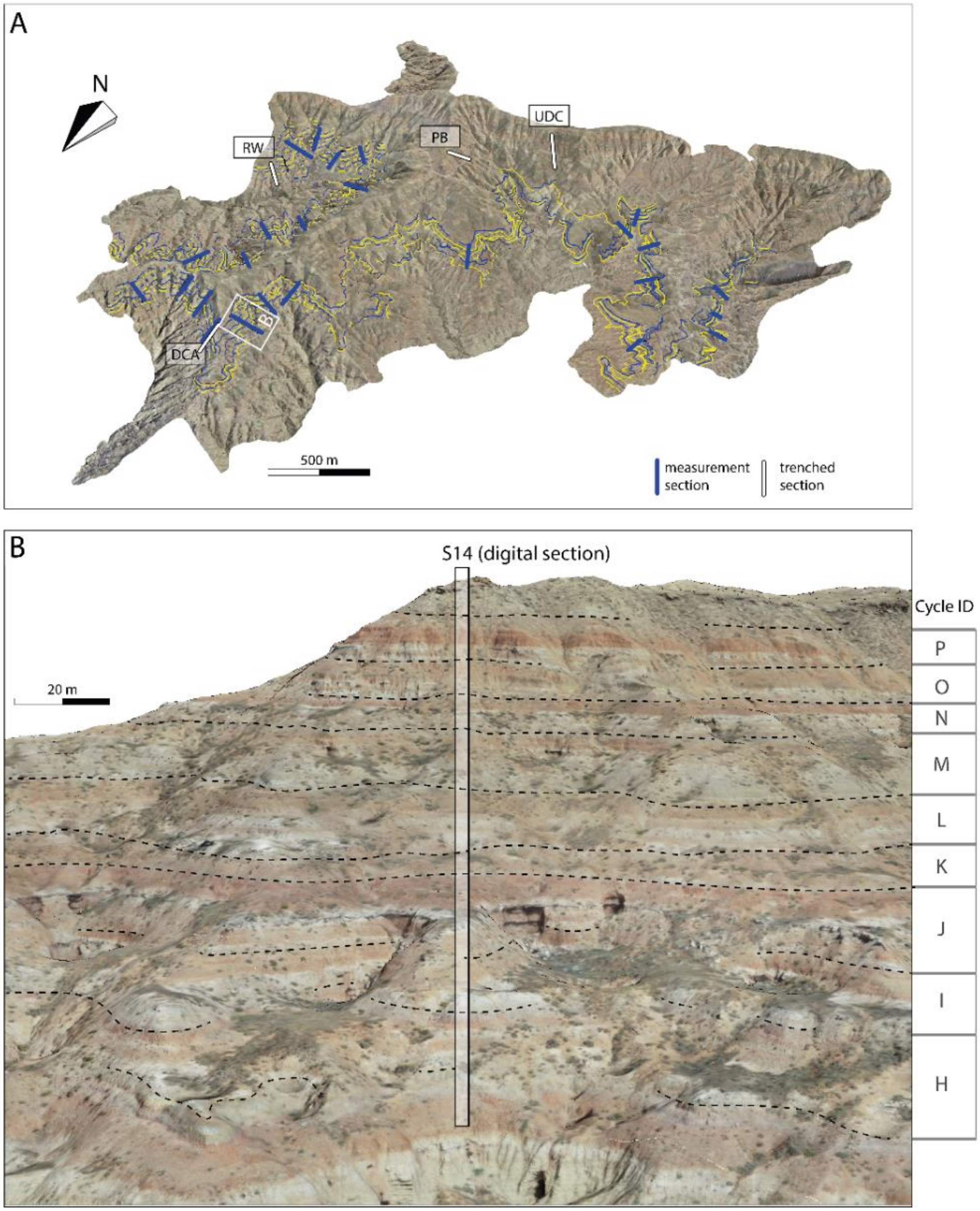

Figure 3. Tracing of floodplain aggradation cycles in the photogrammetric model with the aid of individual drone and camera photos. (A) An overview of the interpreted 3-D photogrammetric model in the McCullough Peaks area, showing traced boundaries for seven successive cycles. (B) A zoomed-in outcrop section in the 3-D model, showing how cycle boundaries (blue and yellow lines) are traced and how a digital section (S14) is constructed.

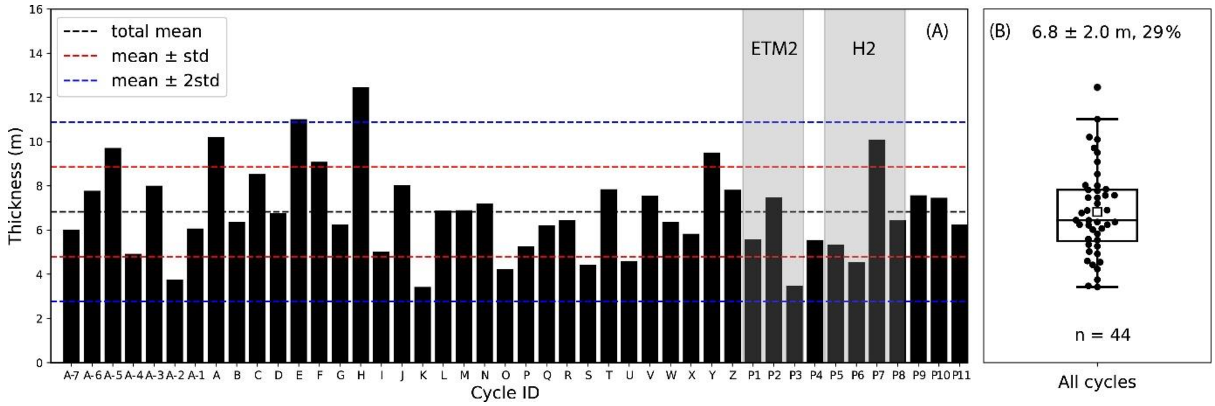

Figure 4. Thicknesses of 44 cycles in the composite stratigraphy. (A) Bar diagram showing the labeling system and cycle thickness variability. (B) Boxplot showing the mean (6.8 m), standard deviation (2.0 m), and CV (standard deviation/mean; 29%) of thicknesses of these 44 cycles. Box boundaries indicate lower and upper quartiles, lines extending from boxes represent the 1st to 2nd and 3rd to 4th quartile ranges, lines and squares within boxes indicate median and mean values, and points outside boxes stand for outliers.

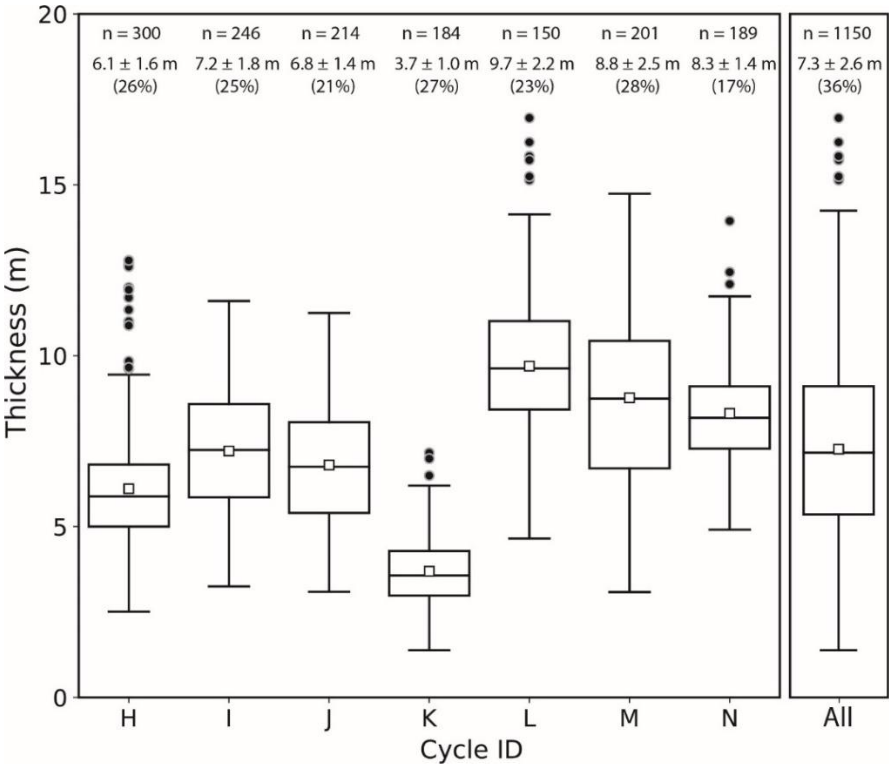

Figure 5. Box plots illustrating the variability of the thicknesses of cycles H-N. The very right boxplot is based on 1150 measurements that are equally contributed by the seven cycles by randomly selecting 150 measurements from each cycle. See explanations of boxplot components in Figure 6. Note that: the number combination of “a ± b (c)” above each boxplot means “average ± standard deviation (CV)”.

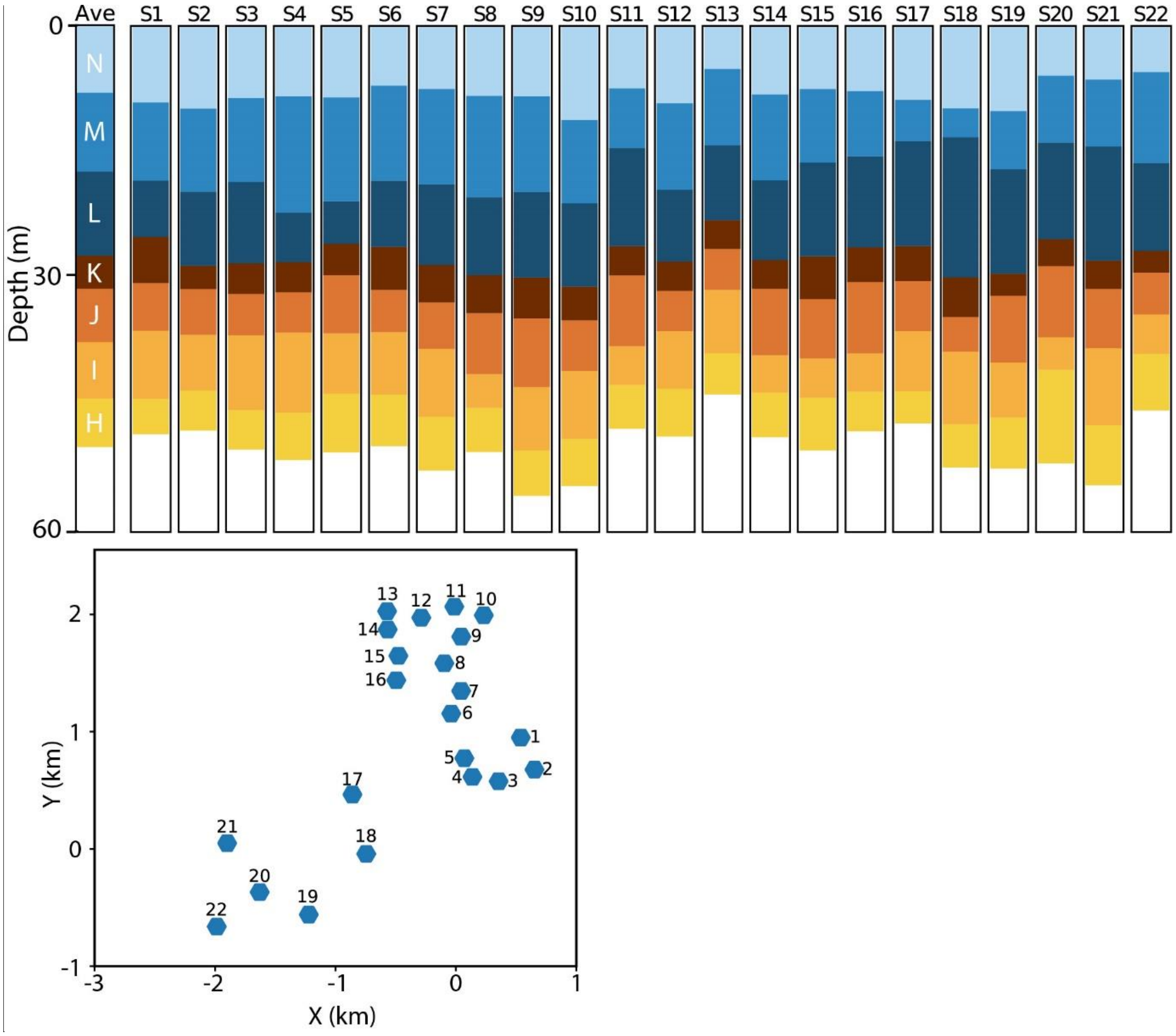

Figure 6. Variation of cycle thickness in the lateral extent. The lower panel shows locations of 22 digital sections, while the upper panel shows the thickness variations of seven successive cycles, with the top cycle flattened. Note that the coordinates in the lower panel are converted from global UTM coordinates to local ones, with the applied offset of X_offset = 673000 m and Y_offset = 49242600 m.

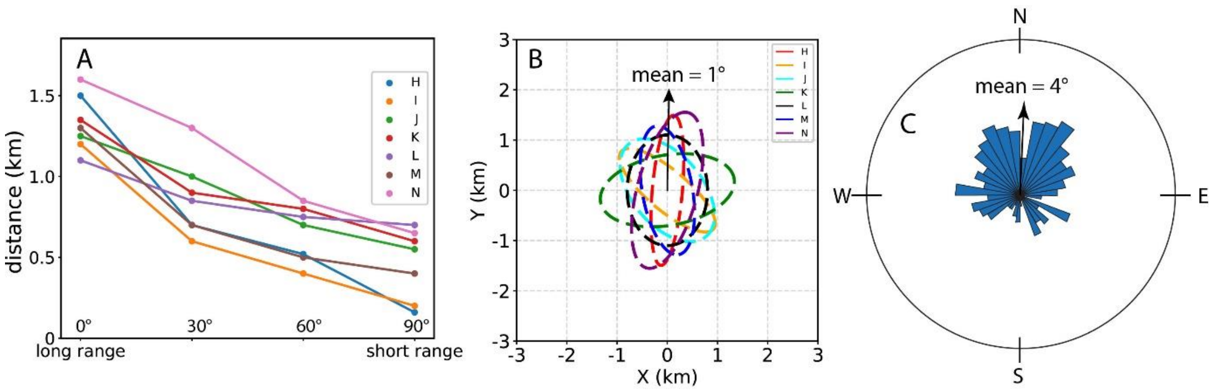

Figure 7. (A) Variation of ranges with azimuth, assuming the long-range azimuth to be N 000° and thus the short-range azimuth to be N 090°. (B) Oriented variogram ellipses with long and short ranges as long and short axes. (C) Field-measured paleoflow directions in the dune-scale cross-stratifications.

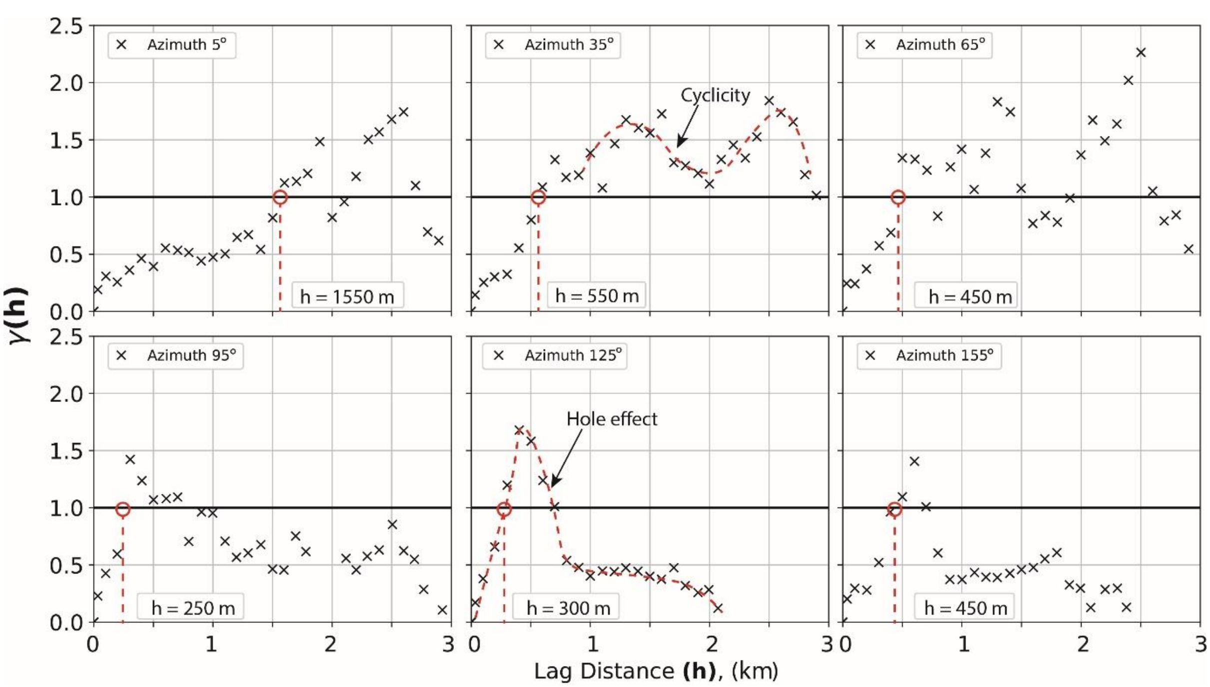

Figure 8. One-dimensional directional variograms for cycle H with different azimuths. Red circles and lines indicate the ranges along different azimuths. Information on how to read variograms has been detailed in Section 3.4.

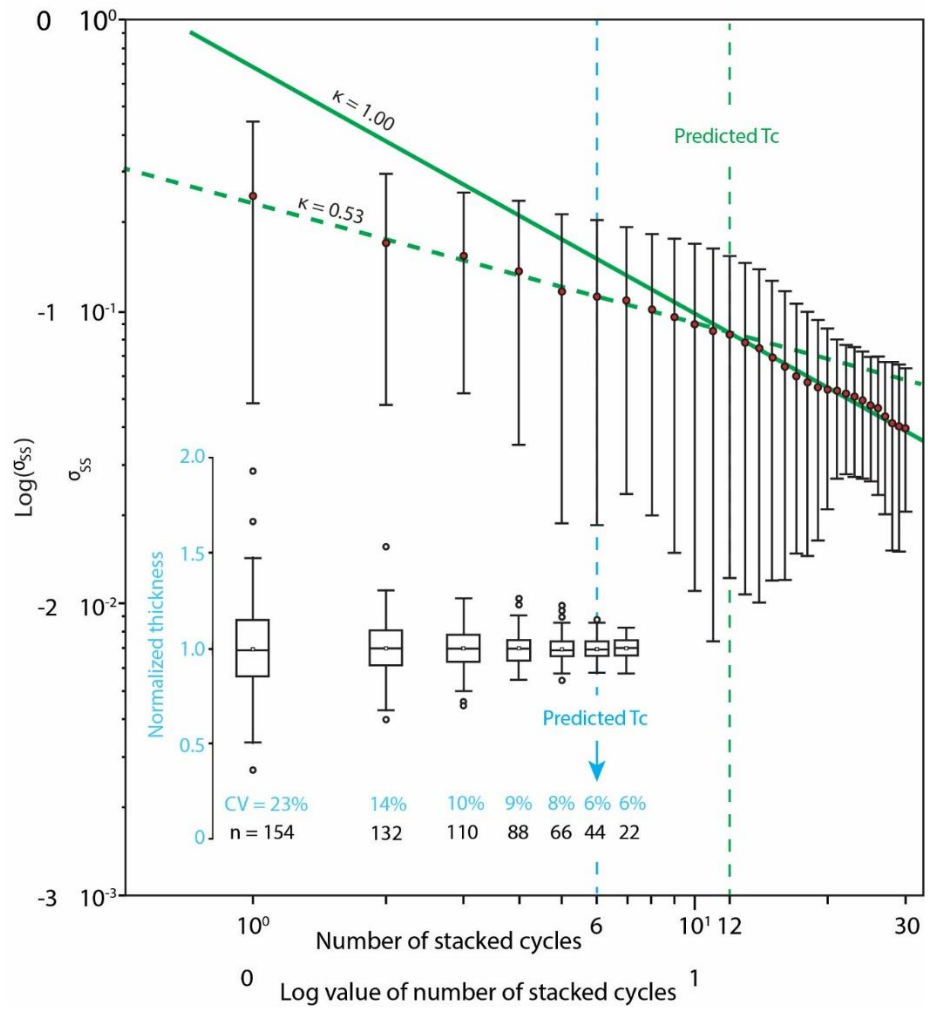

Figure 9. Two metrics for indicating the compensational timescale (Tc). (1) The lower part shows the decay of CV with an increasing number of cycles in a stratigraphic assemblage. The predicted Tc corresponds to about 6 cycles since CV doesn't reduce anymore and stabilizes at 6%. (2) The upper part shows the decay of σ_{ss} with an increasing number of cycles in the composite section (Figure 6). Error bars represent the geometric standard deviation, red dots indicate the average σ_{ss} at the corresponding number of cycles, green dashed trend lines represent the best linear-fit, and the vertical green dashed line indicates the predicted Tc (see Straub et al., 2009 and Section 3.5.2 for a more detailed explanation of the principle) that corresponds to 12 cycles, over which the stratigraphic stacking transits from anti-compensational to compensational form.

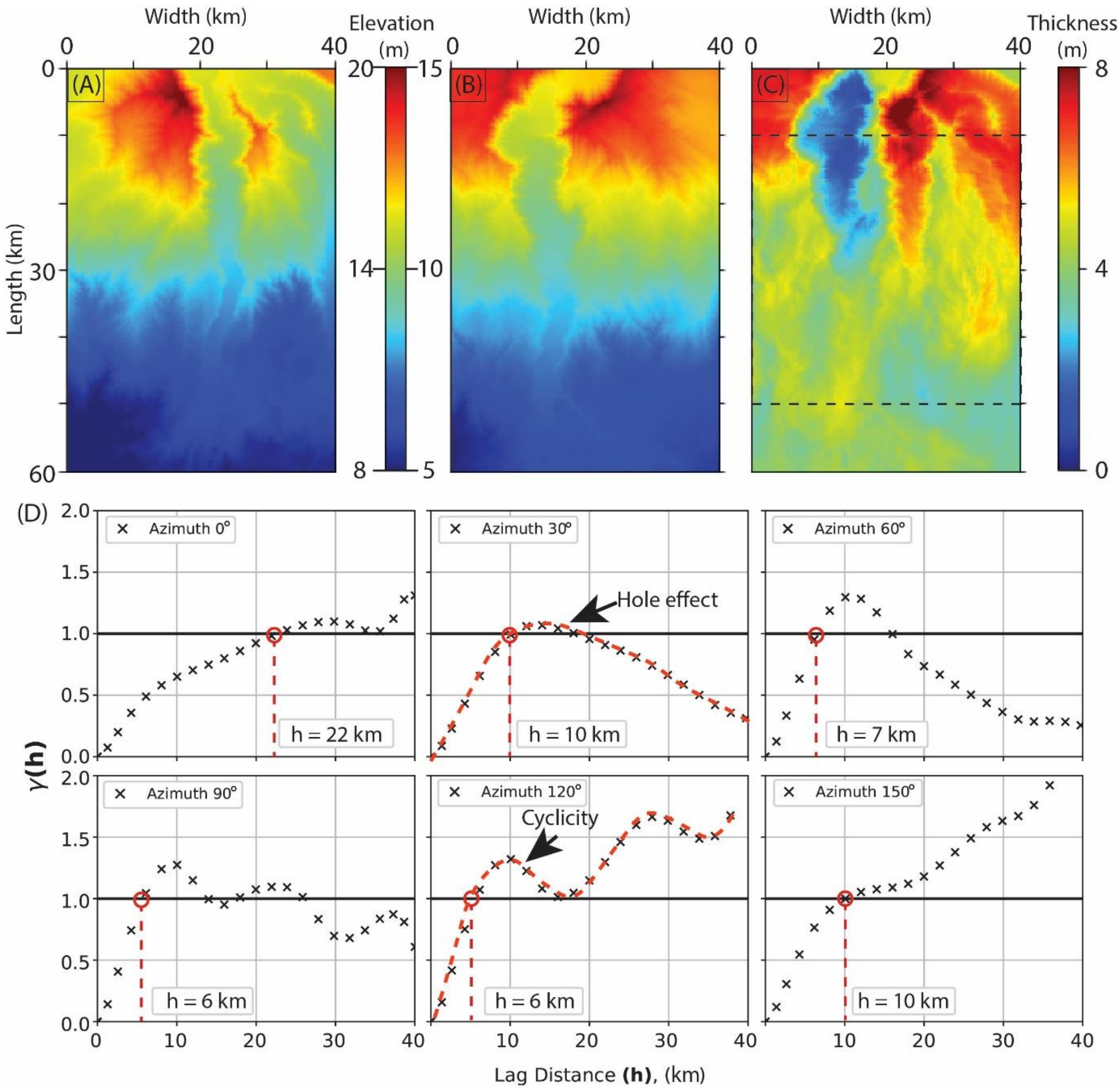

Figure 10. Geostatistical analysis using the Scenario A40 data produced by Wang *et al.* (2021a). (A) The elevation map of the base of cycle 3. (B) The elevation map of the top of cycle 3. (C) The thickness map of cycle 3. (D) Directional variograms using the data constrained in the red rectangular of Figure 10C.

Earth and Planetary Science Letters

Supporting information for:

Spatial characteristics and kinematics of floodplain aggradation cycles in the lower Eocene Bighorn Basin, Wyoming, USA

Youwei Wang[1,2], Timothy F. Baars[1], Joep E.A. Storms[1], Allard W. Martinius[1,3], Philip D. Gingerich[4], Magda Chmielewska[5], Simon J. Buckley[6], and Hemmo A. Abels[1]*

[1] Department of Geosciences and Engineering, Delft University of Technology, Stevinweg 1, 2628 CN Delft, the Netherlands

[2] Department of Environmental Sciences, University of Virginia, Charlottesville, VA 22903, USA

[3] Equinor ASA, Arkitekt Ebbellsvei 10, N–7053 Trondheim, Norway

[4] Museum of Paleontology, University of Michigan, Ann Arbor, MI 48109-1079, USA

[5] Department of Geology and Petroleum Geology, University of Aberdeen, Aberdeen AB24 3UE, UK

[6] NORCE Norwegian Research Centre AS, P.O. Box 22, N-5838 Bergen, Norway

**Correspondence email: youweiwang2021@outlook.com*

This PDF file includes:

Text S1: More detailed principles and workflow for variogram calculation in addition to those in Section 3.4.

Text S2: More detailed workflow about CV calculation in addition to those in Section 3.5.1.

Text S3: More detailed workflow about the calculation and application of compensational stacking index in addition to those in Section 3.5.2.

Figures S1 to S3: References for citations of supporting information

Table S1: Geostatistic features of thicknesses of different floodplain aggradation cycles

Supplementary Information: References

References cited in this supplementary document.

1. Supplementary Information: Texts

Text S1: More detailed principles and workflow for variogram calculation in addition to those in Section 3.4

In addition to the description in the main text and Figure S2, we refer the readers to the following websites for more details about the principle and workflow of variogram calculation.

The website of Eric Kim: https://aegis4048.github.io/spatial-simulation-1-basics-of-variograms

The YouTube channel of Michael Pyrcz: https://www.youtube.com/watch?v=jVRLGOsnYuw

Text S2: More detailed workflow about CV calculation in addition to those in Section 3.5.1

For a stratigraphic interval that has 3 sedimentary cycles, there are three types of assemblages, including assemblages containing only 1 cycle (i.e. Cycle 1, Cycle 2, and Cycle 3), assemblages containing 2 cycles (i.e. Cycle 1 + Cycle 2 and Cycle 2 + Cycle 3), and an assemblage containing 3 cycles (i.e. Cycle 1 + Cycle 2 + Cycle 3). Before calculating the CV, the thicknesses of all assemblages are rescaled by dividing the thickness over the regionally averaged mean of each assemblage. For example, when calculating the CV of the assemblages containing two cycles, we use the following equations

$$AB_{rescaled} = \{\frac{a1+b1}{\bar{a}+\bar{b}}, \frac{a2+b2}{\bar{a}+\bar{b}}\} \quad (S1)$$

$$BC_{rescaled} = \{\frac{b1+c1}{\bar{b}+\bar{c}}, \frac{b2+c2}{\bar{b}+\bar{c}}\} \quad (S2)$$

$$Assemblage\_2 = \{AB_{rescaled}, BC_{rescaled}\} \quad (S3)$$

$$CV_{\mathrm{Assemblage\_2}} = \frac{std(\mathrm{Assemblage\_2})}{1} \tag{S4}$$

where Assemblage_2 has two components, namely Cycle 1 + Cycle 2 and Cycle 2 + Cycle 3; AB_{rescaled} and BC_{rescaled} refer to the sets of rescaled thicknesses of Cycle 1 + Cycle 2 and Cycle 2 + Cycle 3, respectively; std means standard deviation.

In this context, as the number of cycles that comprise an assemblage grows, it is expected that the thickness variation over the study area should become smaller. By some point, we define that the assemblage is fully compensated when the CV value stops decreasing and stabilizes.

Text S3: More detailed workflow about the calculation and application of compensational stacking index in addition to those in Section 3.5.2

To practically identify Tc based on 1-D data, the following workflow can be implemented:

(1) draw a line with a slope of -1 (i.e. $\kappa = 1$);
(2) move this line over the data points to best fit the larger-value parts of the dataset;
(3) identify the knickpoint where the leftmost data point can't be fit by this line with a slope of -1 (i.e. $\kappa = 1$);
(4) observe the data points on the left of this knickpoint and get the slope of a new line that best fits the data points (this line has a slope of $-\kappa'$);
(5) compare the value of $-\kappa'$ with values in Figure 2 by Straub & Wang (2013) to see how large the stratigraphy is influenced by autogenics.

2. Supplementary Information: Figures

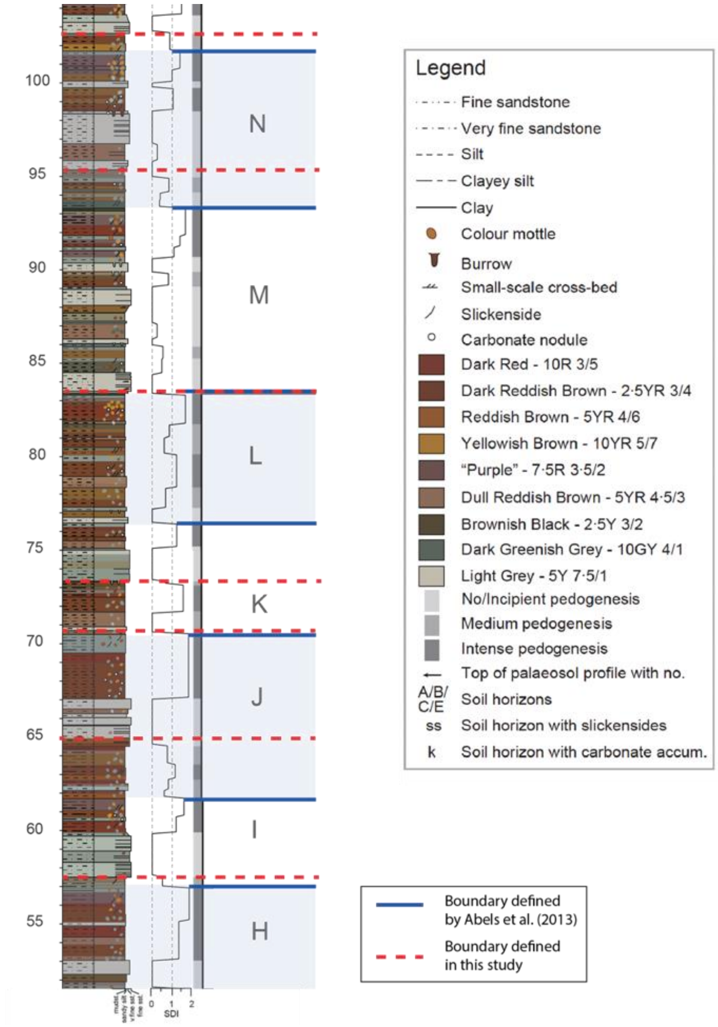

Figure S1. Comparison between floodplain aggradation cycle boundary in this study (red dash line) and that in Abels *et al.* (2013) (blue solid line), taking cycles H-N as examples. The SDI used in this figure is abbreviated for the Soil Development Index (Abels et al., 2013), which is a function of three parameters: palaeosol B horizon thickness, intensity of horizon development, and rubification of the B-horizon. In Abels *et al.* (2013), cycle boundaries are put at the sharpest transition in the soil development index (SDI) curve, which often corresponds to the top of the reddest soil. In contrast, this study places the cycle boundary at the facies transition from reddish/purple overbank deposits to yellowish heterolithic deposits. Note that the cycle boundary in this study is not determined based on this 1D log, but on a regional basis.

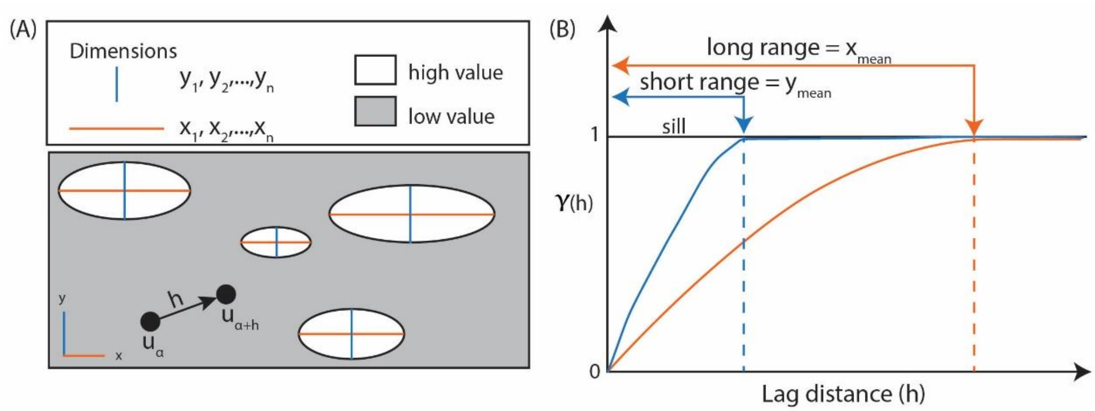

Figure S2. Schematic illustration of variogram components (modified from Pyrcz & Deutsch, 2003). (A) There are lenses with high values in the low-value background, with various long axes (orange horizontal lines with lengths of x_1, x_2, ..., x_n, averaging x_{mean}) and short axes (blue vertical lines with lengths of y_1, y_2, ..., y_n, averaging y_{mean}); (B) The long and short ranges corresponding to x_{mean} and y_{mean} of the high-value lens in Figure S2A, indicating the maximum distance of confident correlation and thus reflecting the spatial continuity of these lenses. Observations appear independent (i.e. variance no longer increases) when the lag distance is beyond the range, indicating non-correlation between a pair of two points when the distance between them is larger than the range.

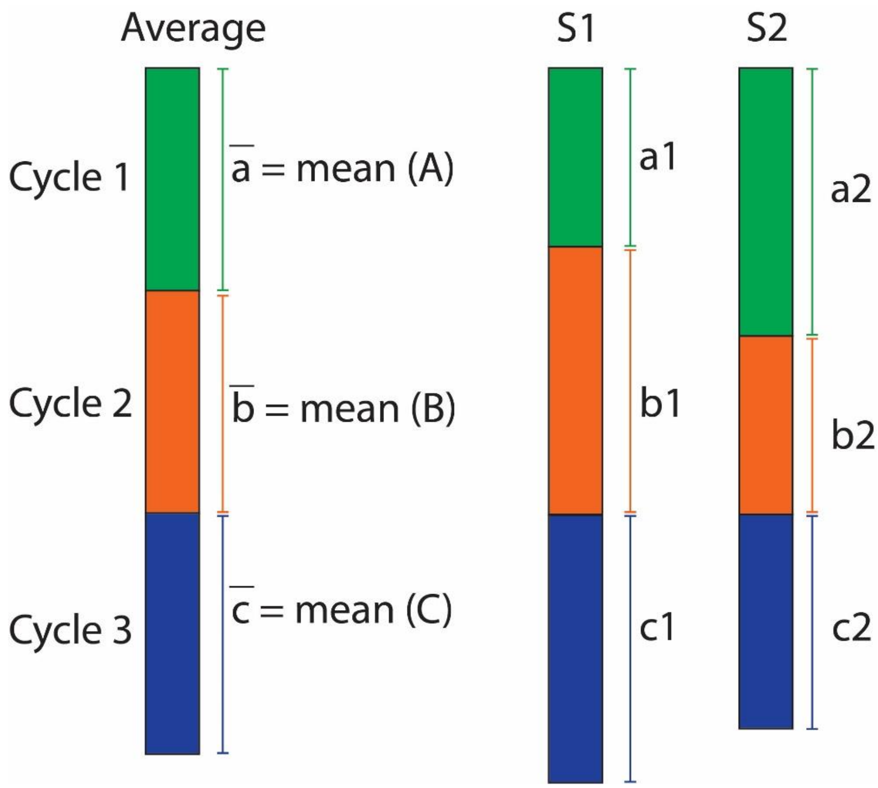

Figure S3. An example showing how CV is calculated for different amounts of cycles that are stacked to form stratigraphic assemblages. S1 and S2 are two synthetic sections with three floodplain aggradation cycles respectively. An average section is made by average the thickness of each cycle. More explanations of the workflow have been presented in supplementary Text S2.

3. Supplementary Information: Tables

Table S1. Geostatistic features of thicknesses of different floodplain aggradation cycles

Cycle ID	Short range (km)	Long range (km)	Aspect ratio	Long-range azimuth
N	0.6	1.6	2.7	15°
M	0.5	1.3	2.6	350°

L	0.8	1.1	1.4	5°
K	0.7	1.4	2.0	80°
J	0.7	1.2	1.7	320°
I	0.4	1.2	3.0	310°
H	0.3	1.6	5.3	5°
Average	0.6	1.3	2.2	1°

4. Supplementary Information: References

Abels, H.A., **Kraus, M.J.** and **Gingerich, P.D.** (2013) Precession-scale cyclicity in the fluvial lower Eocene Willwood Formation of the Bighorn Basin, Wyoming (USA). *Sedimentology*, **60**, 1467–1483.

Pyrcz, M. and **Deutsch, C. V.** (2003) The whole story on the hole effect. *Geostatistical Association of Australasia, Newsletter*, **18**.

Straub, K.M., **Paola, C.**, **Mohrig, D.**, **Wolinsky, M.A.** and **George, T.** (2009) Compensational Stacking of Channelized Sedimentary Deposits. *J. Sediment. Res.*, **79**, 673–688.